Small-scale features of temperature and salinity surface fields in the Coral Sea

Christophe Maes,[1] Boris Dewitte,[1] Joël Sudre,[2] Véronique Garçon,[2] and David Varillon[3]

[1] The small-scale features in sea surface temperature and salinity fields (SST and SSS) of the Coral Sea are examined using high horizontal spatial and short-term temporal in situ measurements. These features are extracted from thermosalinographs (TSGs) gathered onboard commercial and research vessels and at one long-term fixed station. The analyses are performed along the vessel tracks and the structures of small-scale features are extracted by high-pass spatial filtering the original TSG data. For SSS, it is shown that the features at the scale of mesoscale eddies (∼100 km) vary from about −1.1 to +0.6 psu in the Coral Sea region. Processes sustaining such range include rainfall events, stirring by mesoscale eddies, and the latitudinal displacement of the sharp front associated with the edge of the Western Pacific Warm Pool at the seasonal time scales. The TSG data have revealed the presence of a sharp front (0.4–0.6 psu) between the subtropical and equatorial waters instead of a smooth gradient in the standard SSS climatologies. Within the context of recent remotely sensed observations of salinity, this could represent an important limitation for the validation and calibration of satellite products. In addition to these spatial considerations, temporal variations at one long-term station near Vanuatu show that the coupled air-sea responses to intraseasonal tropical variability, such as the Madden-Julian Oscillation, may have a signature in both SST and SSS fields. However, this response is found to be complex and not necessarily in phase. In the Coral Sea region, our results suggest that MJO-induced variability on SST and SSS exhibit little coherency at the seasonal time scales.

1. Introduction

[2] Salinity is a fundamental ocean state variable, playing a significant part in determining the oceanic density. There are also several particular ways in which the ocean salinity variability plays a role in the global climate system. For example, at decadal to millennial time scales, salinity has a direct impact on the thermohaline circulation [e.g., *Schmitt*, 1995]. At seasonal to interannual time scales, salinity stratification results in barrier layers within the western equatorial Pacific warm pool that have been shown to impact both the onset and build-up phases of El Niño/ Southern Oscillation (ENSO) events in coupled numerical models [*Maes et al.*, 2002, 2005]. In addition to dynamical effects, salinity changes also affect oceanographic ecosystems and the marine species that dwell within them [*Freeman et al.*, 2012].

[3] A recent study has highlighted the importance of salinity observations in the effort to elucidate the importance of human-induced changes in the climate system. *Pierce et al.* [2012] showed that joint changes in salinity and temperature yield a stronger indicator of human impact on climate than either salinity or temperature alone. However, current knowledge of ocean salinity is still hampered by a scarcity of long-term salinity records. The emergence and worldwide growth of the Argo array since the early 2000s provides the possibility to evaluate salinity variability on seasonal time scales [*Roemmich and the Argo Steering Team*, 2009], but we cannot expect Argo to be effective in resolving small-scale oceanic features, both in terms of space and time (the standard cycle is every 10 days). A hopeful advance in monitoring the sea surface salinity (SSS) is, however, expected with remote sensing with microwave radiometry from satellites [*Klemas*, 2011]. Since the end of 2009, two satellite missions, the Soil Moisture and Ocean Salinity (SMOS) mission, which is part of the european space agency (ESA's) Earth Explorer Missions, and the Aquarius mission, which is a joint project of the United States and the Argentine SAC-D observatory, have been successfully launched and the two teams have begun to produce global maps of SSS [*Reul et al.*, 2013]. Quality controlled in situ observations are of paramount importance for the calibration and validation of satellite measurements. It is equally important to have a good

[1]IRD/LEGOS, Toulouse, France.
[2]CNRS/LEGOS, Toulouse, France.
[3]IRD/US191, Nouméa, France.

Corresponding author: C. Maes, LEGOS, UMR 5566, CNRS/IRD/ CNES/UPS, 18 Ave. Edouard Belin, FR-31400 Toulouse, France. (christophe.maes@ird.fr)

understanding of the various scales of variability, cascading from the mean circulation down through the mesoscale and the submesoscale to turbulent motion [see e.g., *Roemmich and Sutton*, 1998; *Toole and McDougall*, 2001; *Ridgway and Dunn*, 2003].

[4] In their analysis of SSS measurements from several databases, *Bingham et al.* [2002] found that most frequency histograms for the North Atlantic and the tropical Pacific were non-Gaussian, which for the most part, they attributed to anomalous low-salinity values. *Bingham et al.* [2002] suggested that this negative skewness results mainly from rainfall events but they allowed for other possible mechanisms, like the movement of fronts and eddies. They also indicated the possibility of bimodal distributions in frontal regions. Their results could also be affected by limited sample size in some regions and, interestingly, they did note that in the Coral Sea (as defined by a 1° square located at 19–20°S/173–174°E) SSS does have a normal distribution and there are a large number of salinity observations in this region dating back to the 1970s [*Donguy*, 1994]. In the early 1990s, thermosalinographs (TSG) were developed and tested on merchant ships across the Pacific Ocean [*Hénin and Grelet*, 1996]. The TSG produced not only more accurate SST and SSS observations relative to the earlier bucket measurements but also high-frequency sampling at 5 min intervals and the opportunity to resample regions on a regular basis depending on the shipping schedules. These sensors offered the possibility to monitor the SST and SSS variability across the tropical Pacific on interannual and longer time scales [*Ioualalen et al.*, 2003; *Delcroix et al.*, 2011; *Chen et al.*, 2012]. *Barton* [2007] considered smaller scales in the TSG records in his assessment of SST products derived from nine satellite measurements. Early on, *Hénin and Grelet* [1996] documented the different signals in salinity revealed by the high-frequency sampling rate of the TSG data. However, most of the time, the small-scale features have been evaluated in the context of estimating the signal-to-noise ratio required for mapping and gridding the large-scale variability [e.g., *Delcroix et al.*, 2005].

[5] In the present study, the analyses will focus on the small-scale features of SST and SSS fields observed in the eastern Coral Sea in the southwestern Pacific Ocean. Such features result mainly from the nonlinear ocean mesoscale eddies through submesoscale structures, as well as the presence of steep and persistent fronts. We will use TSG data from the Voluntary Observing Ships (VOS) program in conjunction with a unique time series of SST and SSS spanning ~10 years. We will mainly explore small-scale features of O(100) km typically associated with mesoscale geostrophic eddies and time scales associated with phenomena ranging from the daily to the Intraseasonal Tropical Variability (ITV). The focus will be set more on the SSS field to provide circumstantial elements for the validation and calibration of on-going remotely sensed satellite missions. In section 2, we will present the different data sets and describe how they were processed. Section 3 will provide a description of the small-scale features in SSS and SST observed in the region with some identification of the possible underlying mechanisms, and finally, section 4 presents the discussion and conclusion.

2. Data Sets

[6] The TSG data collected from commercial and research vessels are part of the VOS effort to collect, calibrate, and archive high quality controlled measurements. Hereafter, we use only the delayed-mode data distributed by the French Sea Surface Salinity Observation Service (http://www.legos.obs-mip.fr/observations/sss/). The delayed mode takes into account independent measurements of salinity either from water bottle samples collected directly onboard the vessels (systematically operated after 2002) or from colocalized observations from Argo floats (within 50 km and 5 days from the track position). The validation is performed individually for each voyage and each vessel. The correction of systematic bias is done for individual segments, mainly between the primary ports of call (G. Alory, personal communication, 2013). Corrections can be as large as 0.5 psu (the values according to the 1978 practical salinity scale are given in psu for simplification in the rest of the text), especially after long voyages (typically more than 2–3 months), resulting from scouring and fouling of the salinity sensor. In many cases, the bias has a temporal trend and a linear correction could be applied. A problem with this approach is that the calibration may be applied to a segment that traverses a large region (to have a sufficient number of points) that may be characterized by multiple oceanographic environments. We have revisited the calibration of each track using the available in situ observations within the Coral Sea only, and the seasonal amplitude given by the climatology. Based on such ad hoc approach, the salinity records are typically adjusted by about ±0.1 psu (details are provided in Table 1).

[7] In addition to the VOS data, the TSG data collected at the Sabine bank, located ~80 km southwest of Espiritu Santo island in the Republic of Vanuatu (~16°S/166°20′E, Figure 1b), will be considered as an independent time series. The salinity and temperature data were collected every 15 min in conjunction with a tide gauge anchored at a depth of 15 m, for geodetic observations as part of the MOTE-VAS and GEODEVA programs (P.I. Stéphane Calmant and Valérie Ballu, respectively). The sensors are replaced and recalibrated every year, ensuring the control quality of the full time series. Hereafter, we construct a daily time series over the 2000–2008 period and we have compared these data with Argo observations located in a 3° box around the Sabine bank (using only the positions to the west of Santo island). The root mean square (RMS) differences were found to be reasonable with values of 0.91°C and 0.23 psu in temperature and salinity, respectively (the total number of comparison points is 254). There are two periods longer than 15 days without data and where possible we inserted around Argo observations into these periods only. Finally, we constructed the daily time series by filling short gaps with linear interpolation.

[8] In the discussion, we will highlight the salinity distributions as measured by the new satellite missions. The remote sensing data used include the Aquarius Level 3 standard mapped fields of SSS that are gridded and averaged over 7 day periods. The maps are based on retrievals using the Aquarius Combined Active Passive algorithm [*Yueh et al.*, 2012]. For the SMOS data, we used the CATDS/CEC-OS SMOS Level 3 SSS research products gridded and averaged over 10 day periods [*Reul*, 2012]. We also used several

Table 1. Statistics of the TSG Data Collected on Commercial and Research Vessels for 2010 Across the Coral Sea Region[a]

TSG Voyage	Radio and Voyage Codes	Dates	SSS Adjust	SST Adjust	Min/Max for SSS Small-Scale Features	Min/Max for SST Small-Scale Features
V01	3ENY2_b	28–30 Jan	+0.1	+0.53	−0.38 +0.31	−0.45 +0.51
		No Data in Feb to Mar				
V02	3FLZ_d	21–24 Apr	—	+0.40	−0.65 +0.41	−0.60 +0.50
V03	3FLZ_d	31 May 6 Jun	—	+0.40	−0.26 +0.18	−0.54 +0.49
V04	3ENY2_e	4–6 Jun	—	+0.42	−1.12 +0.58	−1.05 +0.66
V05	3FLZ_f	30 Jun 2 Jul	−0.1	+0.20	−0.21 0.17	−0.50 +0.72
V06	FHQB_c	15–16 Aug	+0.05	+0.30	−0.15 0.16	−0.53 +0.41
V07	3ENY2_i	27–30 Sep	−0.1	+0.48	−0.26 +0.19	−0.48 +0.48
V08	FHQB_c	22–25 Oct	−0.05	+0.37	−0.24 +0.20	−0.56 +0.69
V09	3FLZ_j	27–30 Oct	—	+0.15	−0.25 +0.25	−0.61 +0.69
V10	HOWN_b	29 Nov to 2 Dec	−0.1	+0.21	−0.25 +0.29	−0.39 +0.50
V11	3FLZ_l	24–27 Dec	−0.1	+0.37	−0.24 +0.26	−0.45 +0.33

[a]The details for each voyage are given in the first-left three columns, then the SSS and SST adjustments (in psu and °C), and the min-max of the small-scale features for SSS and SST (in psu and °C), respectively.

additional gridded data products as well as standard climatologies as CARS2009 [*Ridgway and Dunn*, 2003] to compare with the aforementioned in situ observations and to place them in a large-scale context. For the SST, the daily product is based on optimum interpolation of data from multiple satellites and is distributed by the national oceanic and atmospheric administration (NOAA) climate data record program [*Reynolds et al.*, 2007]. This product has been also used to calibrate the SST measurements from the TSG sensors. The comparison shows that the TSG data from the vessels have a warm bias ($0.3°C$ in average) due to the fact that the measurement is made with a time delay of several minutes and at some distance the point of intake of the seawater depending on the speed of the vessel. The adjustment made for each voyage in SST is reported in Table 1.

[9] In order to interpret the small-scale features revealed by the TSG observations, different additional data sets will be considered in relation with the suspected mechanisms that are relevant. The daily precipitation rate is computed from the 3B42 algorithm (version 7) applied to data from the Tropical Rainfall Measuring Mission (TRMM). *Huffman et al.* [2007] discussed the evaluation of the precipitation climatology with rain gauge data. To reveal the features related to ocean dynamics, we use the surface currents from the GEKCO estimates with a $1/4$ degree horizontal resolution with global coverage and daily time intervals [*Sudre et al.*, 2013]. Cross validation with the surface velocity derived from the Argo autonomous floats reveal that the GEKCO estimates are satisfactory in the Coral Sea. The transport and stirring associated with the oceanic flow can be characterized using Finite-Size Lyapunov Exponents (FSLE) following the methodology proposed by *Hernandez-Carrasco et al.* [2011, 2012]. The idea is to
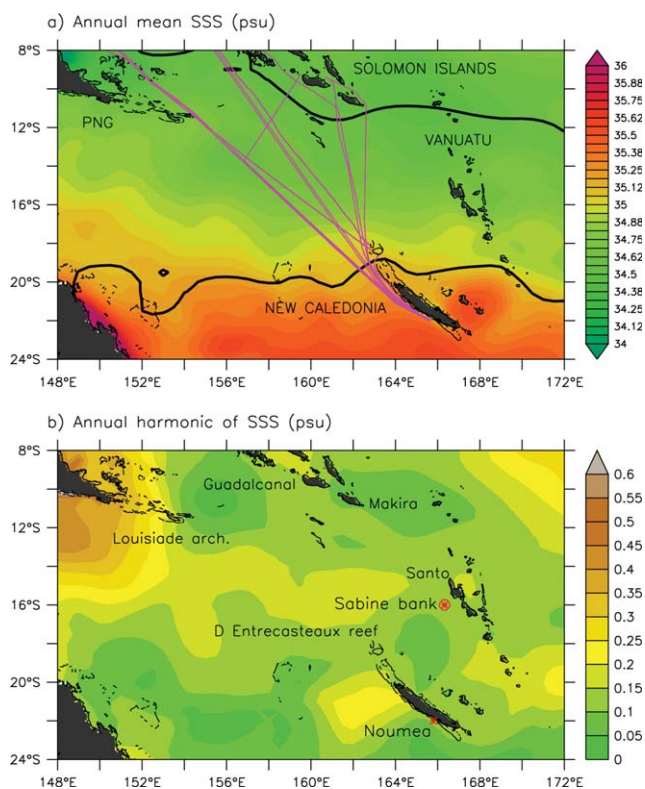

Figure 1. (a) Annual mean SSS and (b) amplitude of the annual harmonic in the eastern Coral Sea region from the CARS2009 climatology [*Ridgway and Dunn*, 2003]. (top) The along tracks of the TSG data are superimposed (in purple) as well as the maximal extension of the $28°C$ isotherm (black thick lines). (bottom) The position of the Sabine bank is indicated by the red symbol.
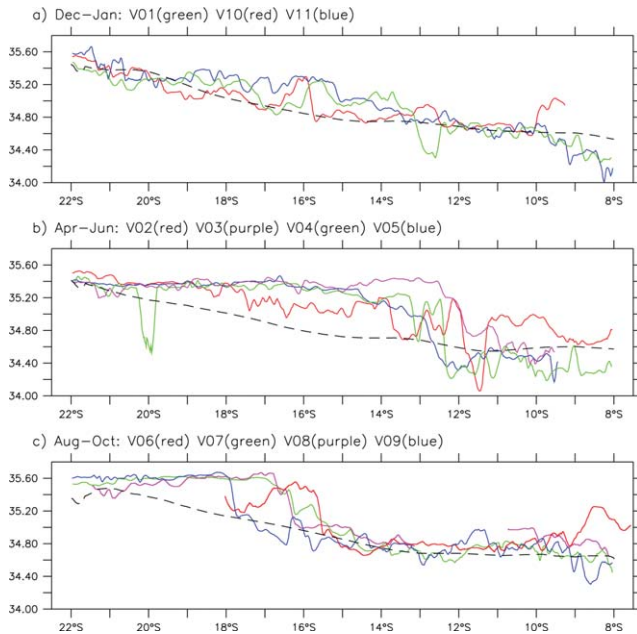
Figure 2. Along track high-resolution SSS data from TSG measurements for the (a) December to January, (b) April to June, and (c) August to October time periods of 2010. The dashed line in each figure represents the CARS2009 climatology interpolated to the mean position of the different TSG data. Note that the V08 voyage has two legs with some missing values near 12°S.

Figure 3. Along track high-resolution SST data from TSG measurements for the (a) December to January, (b) April to June, and (c) August to October time periods of 2010. The dashed line in each figure represents the SST field from *Reynolds et al*. [2007] interpolated to the mean position of the different TSG data. Note that the V08 voyage has two legs with some missing values near 12°S.

determine the dispersion of a pair of particles as they are transported by the flow. For example, as we are interested by the mesoscale flow, the initial separation of the particles is set to 0.025° and the final separation specified as 1°. The FSLE method will determine the time lapse for two particles at the initial separation to achieve the final separation. It thus gives time scales for dispersion and stirring and it also allows the identification of so-called Lagrangian Coherent Structures (LCSs), i.e., persistent structures that organize the fluid transport of properties and of floating material, whether marine pollution or living resources [e.g., *Sudre et al*., 2013]. Here we employed a backward time sequence, so the computation of FSLE depicts the LCS associated with the divergence of the flow.

[10] To interpret the high-frequency temporal variations in the TSG data at the Sabine bank, we use an index of the Madden and Julian Oscillation (MJO) that represents the main mode of intraseasonal atmospheric variability in this region [*Madden and Julian*, 1972]. We consider an index that had been proposed by *Wheeler and Hendon* [2004] (http://cawcr.gov.au/staff/mwheeler/maproom/RMM/). Briefly, it is based on the first two Empirical Orthogonal Functions (EOFs) of the combined fields of near equatorially averaged 850 hPa zonal wind, 200 hPa zonal wind, and satellite-observed outgoing longwave radiation (OLR) data. The MJO amplitude/variance index is then calculated from the 91 day running variance of the modulus of the first two EOFs (i.e., $\sqrt{RMM1^2 + RMM2^2}$). The result is an index of the periods of high and low MJO activity.
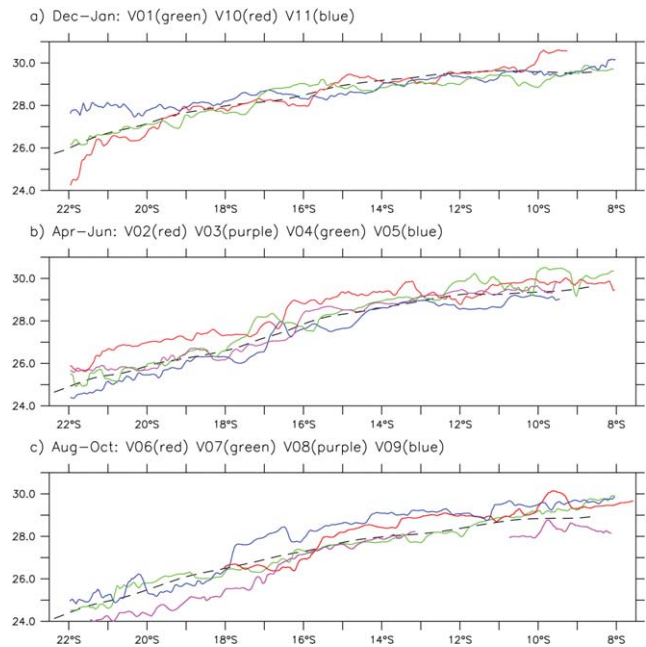
3. Results

[11] To maximize spatial resolution, we keep the 5 min sampling frequency of the TSG records collected by vessels. The data were collected along tracks across the Coral Sea in 2010, from Nouméa near 22°S to the islands within the Solomon Sea and southward of 8°S. The routes used by the different vessels are all on the lee side of the islands with respect to the trade winds, paralleling the western coast of New Caledonia, joining the Solomon Sea across the zonal section between the Louisiade archipelago of Papua New Guinea and Makira Island in the Solomon Islands, following approximately the 11°S latitude (Figure 1). With typical speeds of the merchant ships (15–20 kn), it takes between 2 and 3 days to complete the sections of SST and SSS shown in Figures 2 and 3, which thus may be seen as quasi-daily snapshots of the surface conditions. We use these sections to characterize the spatial scales but it should be kept in mind that some temporal aliasing of the records, for example, by the diurnal cycle, is possible.

[12] Overall, the combined general structure of the SST and SSS fields show a trend from relatively cool and salty subtropical water (T < 28°C, S > 35 psu) in the south to relatively warm and fresh Solomon Sea water (T > 28°C, S < 35 psu) in the north. The SST field exhibits a relatively smooth gradient year round from south to north with a seasonal cycle on the order of 4–5°C southward of about 18°S. The SSS field, on the other hand, shows a very different kind of behavior during the April to October period. Instead of a smooth gradient, there is a steep front as large as of 0.6 psu, separating subtropical water of nearly constant salinity
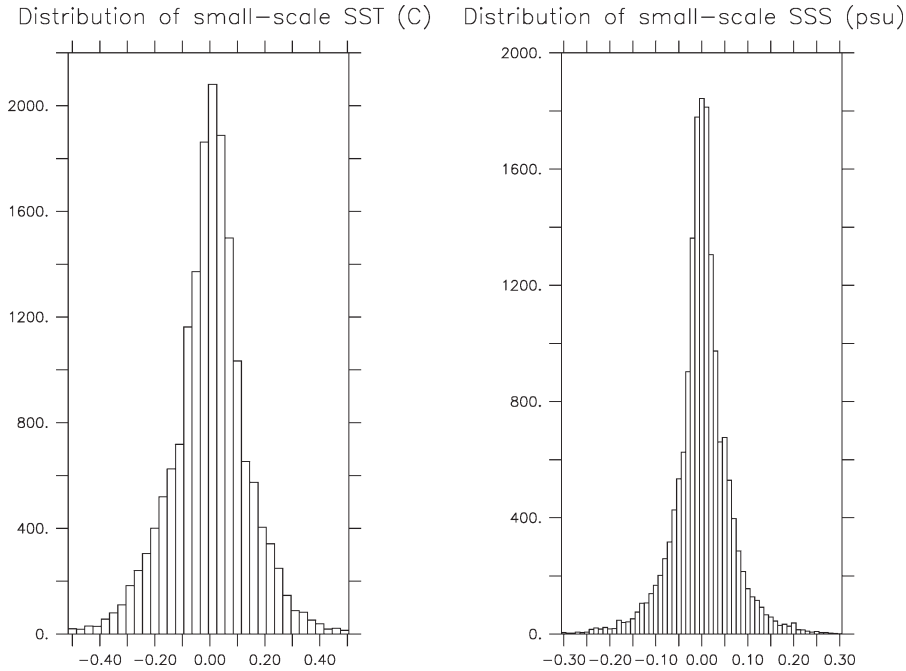
Figure 4. Frequency distribution of the small-scale features of (left) SST (in °C) and (right) SSS (in psu) fields of the TSG data collected along the vessel tracks as shown in the Figure 1a.

from the fresher waters of the Solomon Sea. This frontal separation extends southward from the Solomon Sea boundary near 12°S (Figure 2b) to the D'Entrecasteaux reef marking the north end of the New Caledonian Reef near 18°S (Figure 2c). During the austral summer, the front is not so clearly marked and is replaced by a smooth gradient in good agreement with the CARS2009 climatology (dashed lines in Figure 2; see also the background field in Figure 1a). The sharp fronts that we see in the quasi-synoptic SSS sections are also absent from the other climatologies we have examined, all of which show smooth gradients between the salty subtropical waters and the fresh

Figure 5. Temperature-Salinity diagram for the TSG data of the V04 (green) and V05 (blue) voyages. The black lines are the iso-density (every 0.2 kg/m³).

Solomon Sea waters. These frontal values are also much larger than the amplitude of the annual harmonic depicted by climatologies (Figure 1b). For instance, in the 18–12°S/ 158–162°E region, the averaged annual harmonic is equal to 0.15 psu, explaining more than 90% of the seasonal variations in the CARS2009 climatology. Thus, the differences between the synoptic observations and the climatologies may be as large as 0.4–0.5 psu across distances of 4–5° in latitude. If SSS retrieval algorithms for satellite measurements must fall back on climatological fields in many parts of the oceans, it will be important to document the SSS features in areas where fronts represent important features.

[13] We extracted the small-scale features along each individual vessel track by removing a smoothed record made by passing the original data through a 6-h boxcar filter (some examples of the resulting small-scale features during a voyage are shown in (top) Figures 6 and 7. We plotted frequency histograms of the resulting small-scale features in SST and SSS in the Figure 4. Both histograms appear to be normally distributed. In SSS, the largest amplitudes in the small-scale features are nevertheless found to be negative for most of the voyages across the Coral Sea (Table 1). Taken into account all the voyages together, it results into negative skewness with −0.20 for SST and −1.20 for SSS (at the 90% confidence level) for the distributions as shown in Figure 4. It may be expected that SSS will have shorter scales than SST because it lacks a direct feedback loop with the atmospheric fluxes. For SSS, the main departure from a normal distribution is due to anomalous low-salinity measurements. In the tropical areas, it is known that strong local precipitation can cause a sharp drop in SSS. A good example is the 0.8–1.0 psu drop near 20°S along the V04 voyage which occurred during the month of June (the green curve in Figure 2b). Daily maps of the 3B42 precipitation during the same period show high
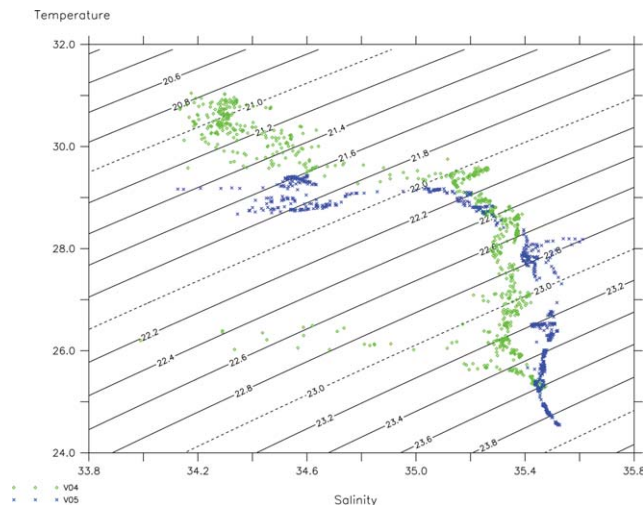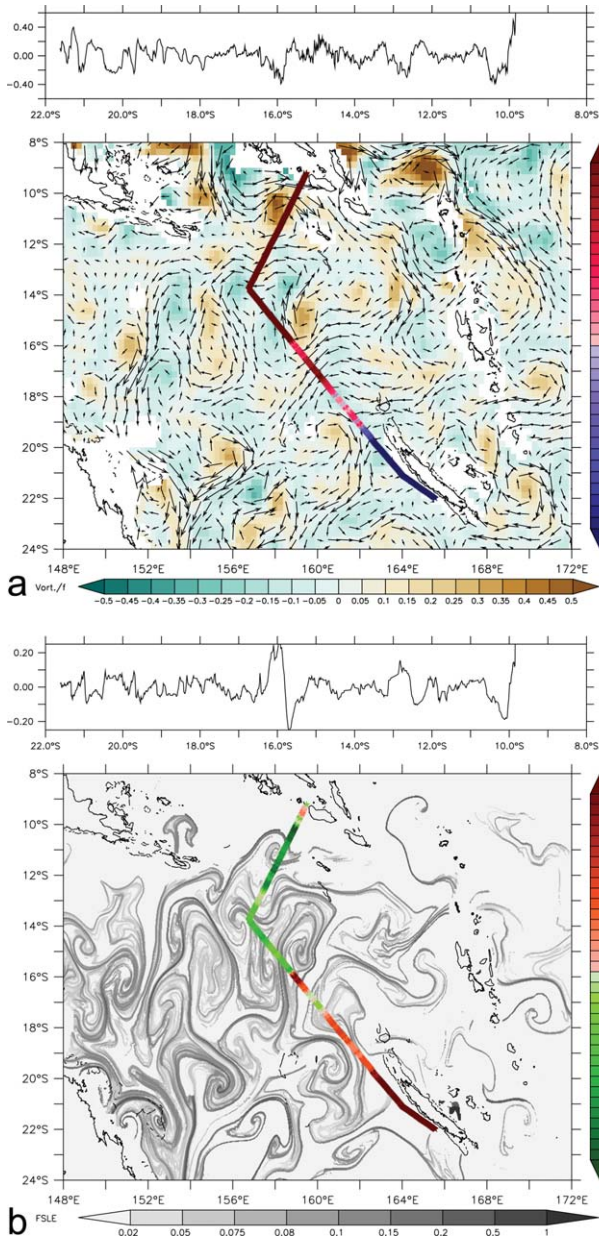
of V04 is also shown in Figure 5 with a density drop larger than 1 kg/m³.

[14] The T-S diagrams exhibit another type of variability where correlated changes in temperature and salinity occur in a compensating manner with little or no change in density. In most of these cases, the changes are characterized by an increase in salinity compensated by a warmer temperature, the size of these variations being typically small, on the order of 0.2 psu in SSS and 0.5°C in SST (for instance, see the compensating effect near the 22 kg/m³ for the V04 voyage in Figure 5). Another type of signal corresponds to changes in density resulting from the combined effect of salinity and temperature and indicating a significant shift in the background oceanic environment or in comparison of the standard climatologies along the track.
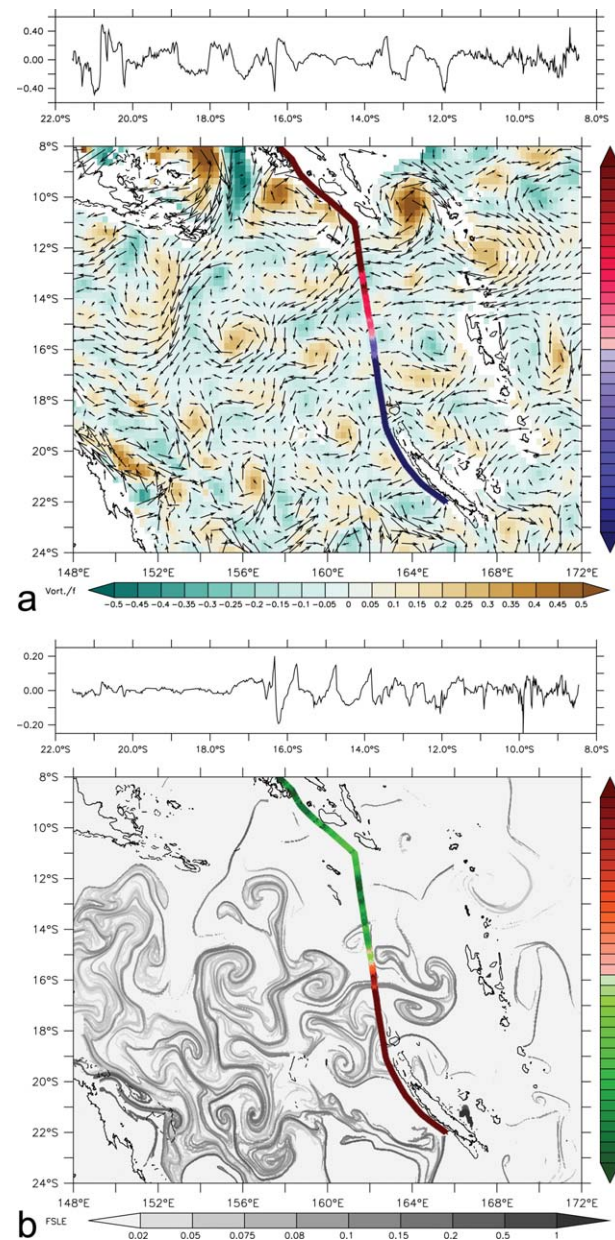

Figure 6. (a) (top) Small-scale features of SST (°C) and (bottom) relative vorticity scaled by f (shade with the bottom color bar) associated with the GEKCO surface currents (vectors) and the TSG SST along the track of the V10 voyage (in °C, shade with the color bar on the right). (b) (top) Small-scale features of SSS (psu) and (bottom) FSLE field (in days⁻¹, shade with the bottom color bar) and the TSG SSS field along the track for the V10 voyage (in psu, shade with the color bar on the right).

rainfall totals, locally greater than 100 mm, which were associated with the movement of a cyclonic depression emanating from the northwestern side of New Caledonia. Not all the individual freshening events could be so easily associated with a particular local rainfall event but vessels also encounter fresh lenses that have persisted from previous events. The signature of such events is unambiguous in surface T-S diagrams, where it appears as an abrupt drop in density with a corresponding drop in salinity. The example

Figure 7. (a) Same as the Figure 6a for the V07 voyage. (b) Same as the Figure 6b for the V07 voyage.
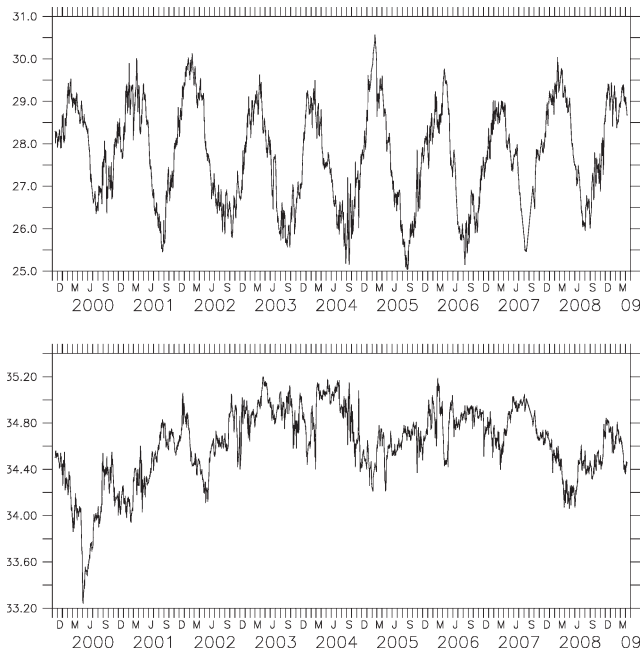
Figure 8. Time series of SST (°C) and SSS (psu) recorded at the Sabine bank (~16°S/166°20′E, see the star in Figure 1b) over the 2000–2008 period.

A good example is represented by the V10 voyage at the end of November where two salinity jumps as large as 0.3 psu occurred between 18°S and 11°S across the Coral Sea (red curve in Figure 2a). Other jumps in salinity also occur across the frontal zone separating the subtropical and tropical waters near 16°S for the V07 voyage (green curve in Figure 2c). To fully interpret these signals, it is necessary to put them back into the horizontal large-scale features of the flow.

[15] By comparing the transect data with the dynamical fields such as the FSLE deduced from the Geostrophic and Ekman Current Observatory (GEKCO) currents, we can place the salinity and temperature variations within the large scale Coral Sea surface circulation (Figures 6 and 7). The fluctuations of salinity on small-scale features result from the stirring of LCSs as depicted by the backward FSLE that are a reflection of the mesoscale eddy activity. The comparisons are done with daily snapshot of the FSLE, at the dates corresponding to the middle transit across the Coral Sea for each voyage. For the V10 voyage, the intrusion of high salinity waters results from interactions between cyclonic and anticyclonic eddies (Figure 6a), resulting in a "triskel structure" where the largest gradients of SSS are associated with typical values of 0.1 day^{-1} in FSLE and of ±0.3 psu in the salinity field (Figure 6b). In comparison, the V07 voyage exhibits a less organized flow (Figure 7a) and weaker features (~0.2 psu) that could be associated with the crossings of the tail of a "mushroom structure" in FSLE in the region between New Caledonia and Vanuatu, near 16°S (Figure 7b). Amplitudes in FSLE associated with these features in salinity are between 0.1 and 0.2 day^{-1} corresponding to a 5–10 days time scale, values that are typical of the region [*Waugh et al.*, 2006].

[16] As mentioned earlier, TSG records from occasional vessels should be considered as quasi-snapshots of the surface conditions and although some tracks may have been occupied closely in time, they are far too few in number to resolve the intraseasonal variability. In the Tropics, a dominant component of the intraseasonal variability is the Madden-Julian Oscillation (MJO) that is associated with air-sea interactions across the equatorial Indian and western/central Pacific oceans with a local period of 30–90 days [e.g., *Hendon*, 2005]. The MJO perturbs the upper ocean through surface fluxes of momentum, latent and sensible heat, radiation, and fresh water and will have consequently a strong seasonal signature in SST and by presumption in SSS. To document the short-term time scales that might be associated with the MJO, we used the time series of daily surface fields recorded at the site of the Sabine bank (Figure 1b) that is shown in Figure 8 for the 2000–2008 period. The time series of the SST field shows a clear seasonal cycle with an amplitude of 4–5°C with values warmer than 28°C in the austral summer, between October and March, which are consistent with the earlier transects shown in Figure 3. The interannual variability is weak as might be expected from the pattern of the dominant interannual mode for SST in the tropical Pacific Ocean that has a zero crossing near the Sabine bank [*Leuliette and Wahr*, 1999]. On the other hand, the SSS seasonal variability is less distinct, showing only a tendency toward low values in the late Austral summer. However, it is clear that the dominant signal in SSS is the interannual variability associated with the displacements of the South Pacific Convergence Zone (SPCZ) and with large-scale precipitation events. *Fisher et al.* [2004] have showed that precipitation in New Caledonia responds nonlinearly to ENSO with a higher correlation with warm moderate central Pacific events and cold La Niña events. We expect this to be true also at the Sabine bank. For confirmation, we calculated the correlation between the interannual SST anomalies at the Sabine bank and the C index defined by *Takahashi et al.* [2011] which accounts for Central Pacific warm events and La Niña events. The maximum correlation is 0.68 at a lag of 2 months (C leading SSS). The positive correlation over this period can be attributed mostly to the cold central Pacific anomalies (i.e., c = 0.55 with C < 0). Both time series exhibit a large amount of high-frequency variability superimposed on the seasonal and interannual variations.

[17] In order to document the intraseasonal features for SSS and SST at the Sabine bank, we first defined the intraseasonal anomalies as the deviation from the monthly mean values that are interpolated to daily values using cubic spline. This technique has been used in a number of studies for documenting the intraseasonal atmospheric variability in the tropics [*Lin et al.*, 2000; *Dewitte et al.*, 2011]. Wavelet decomposition on both time series is then performed following *Torrence and Compo* [1998]. The monthly mean climatology of the normalized wavelet coefficient at each frequency is then calculated, which allows focusing on the seasonal dependence of the intraseasonal activity. Figures 9 and 10 display the results for the time series of SST and SSS, respectively. In the Figure 9b, the Global Wavelet Power Spectrum (GWPS) corresponds to the integral of the wavelet power spectrum over the whole record. It indicates that most of the energy is found in the frequency band
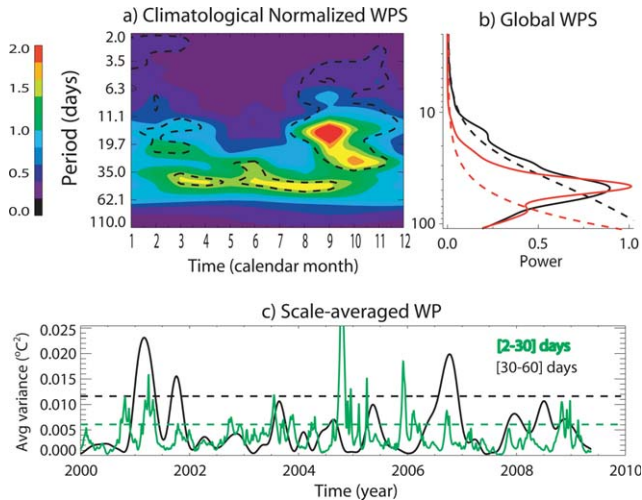
Figure 9. Spectral analysis of the intraseasonal anomalies for SST at the Sabine bank: (a) Climatological Normalized Power wavelet (Morlet) spectrum. The latter consists in a wavelet decomposition of the time series followed by a calculation of the climatology of the Wavelet Power coefficient at each frequency. Wavelet Power was first normalized following equation (14) of *Torrence and Compo* [1998] in order to compare the magnitude of the wavelet power at different frequencies. Scale is indicated on the left, unit in$°C^2$ (scaled by 5.10^{-4}). (b) Global wavelet spectrum in black line. The red line is for the MJO index (RMM1 series, scaled by 0.2). (c) Scale-averaged wavelet power (in $°C^2$) over the ($2-30$ days^{-1}) frequency band (green) and the ($30-60$ days^{-1}) frequency band (black). The dashed lines in all figures represent the 95% confidence level estimated from a red noise (Markov model).

between 30 and 70 days, which corresponds to the frequency range of the MJO. A weaker peak is observed in the frequency range $10-30$ days^{-1}. The climatological Normalized WPS (NWPS) in Figure 9 separates the two regimes of variability more clearly: the $10-30$ days regime that is prominent in austral spring and the $30-60$ days regime that
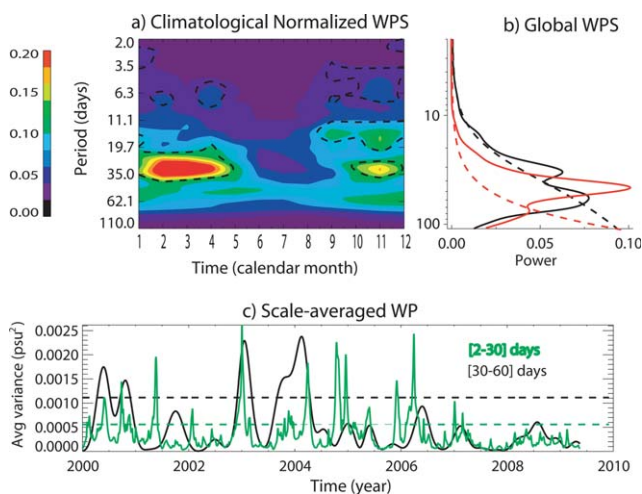

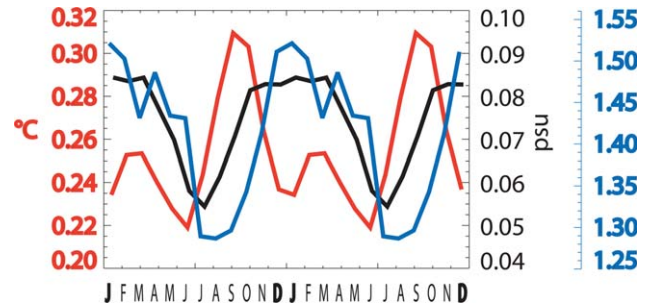**Figure 10.** Same as for the Figure 9 for SSS at the Sabine bank.

Figure 11. Climatological running (91 days) variance of intraseasonal anomalies for SST (red), SSS (black) at the Sabine bank, and MJO (blue). The variance for the MJO is calculated from time series associated to the first two combined EOFs for near equatorially averaged 850 hPa zonal wind, 200 hPa zonal wind, and satellite-observed OLR data [i.e., *Wheeler and Hendon*, 2004].

is prominent during early fall and late Austral winter as is the MJO index (not shown). The NWPS for the SSS time series exhibits a contrasting seasonal cycle (Figure 10a) with relatively more energy in the high-frequency regime than it is case for SST, suggesting the influence of either oceanic processes or high-frequency atmospheric disturbances such as Kelvin and Rossby convective waves. The Global WPS (Figure 10b) still reveals a prominent peak at the MJO time scale, which suggests that both SST and SSS at the Sabine bank are influenced by the MJO. Like SST, the SSS time series also reveals a marked seasonal cycle of its intraseasonal variability with reduced activity in austral winter (Figure 10a). A modulation at interannual time scales is also observed (Figures 9c and 10c), which, however, does not coincide with the MJO amplitude index. The correlation between the MJO amplitude index and the 91 days running variance of the low-pass filtered (fc = 1/30 days^{-1}) SST (SSS) time series is less than 0.18 (0.15). The seasonal modulation of the intraseasonal variability for SSS (Figure 9a) suggests, however, that a relationship with the MJO seasonal variance could exist since it peaks in Austral summer like the MJO [e.g., *Wheeler and Hendon*, 2004]. In order to further document the seasonal dependence of the relationship between SST and SSS at the Sabine bank and the ITV, the climatology of the variance of each field (SST, SSS, and ITV indices) is shown in Figure 11. The figure thus illustrates during which season the intraseasonal variability is stronger or weaker. The intraseasonal activity in SST at the Sabine bank is out of phase with that for the MJO and SSS, which have peaks in austral summer and are reduced in winter. This suggests that there is a larger impact of MJO-induced precipitation (evaporation) on SSS than of MJO-induced wind stress on SST in this particular region.

4. Discussion and Conclusions

[18] In the present study, we analyze in situ measurements from thermosalinograph sensors, mostly hull mounted on commercial and research vessels, but also installed at one fixed platform. The focus has been set on the Coral Sea in the southwest Pacific Ocean. With these data sets, we were able to show that the amplitude of the
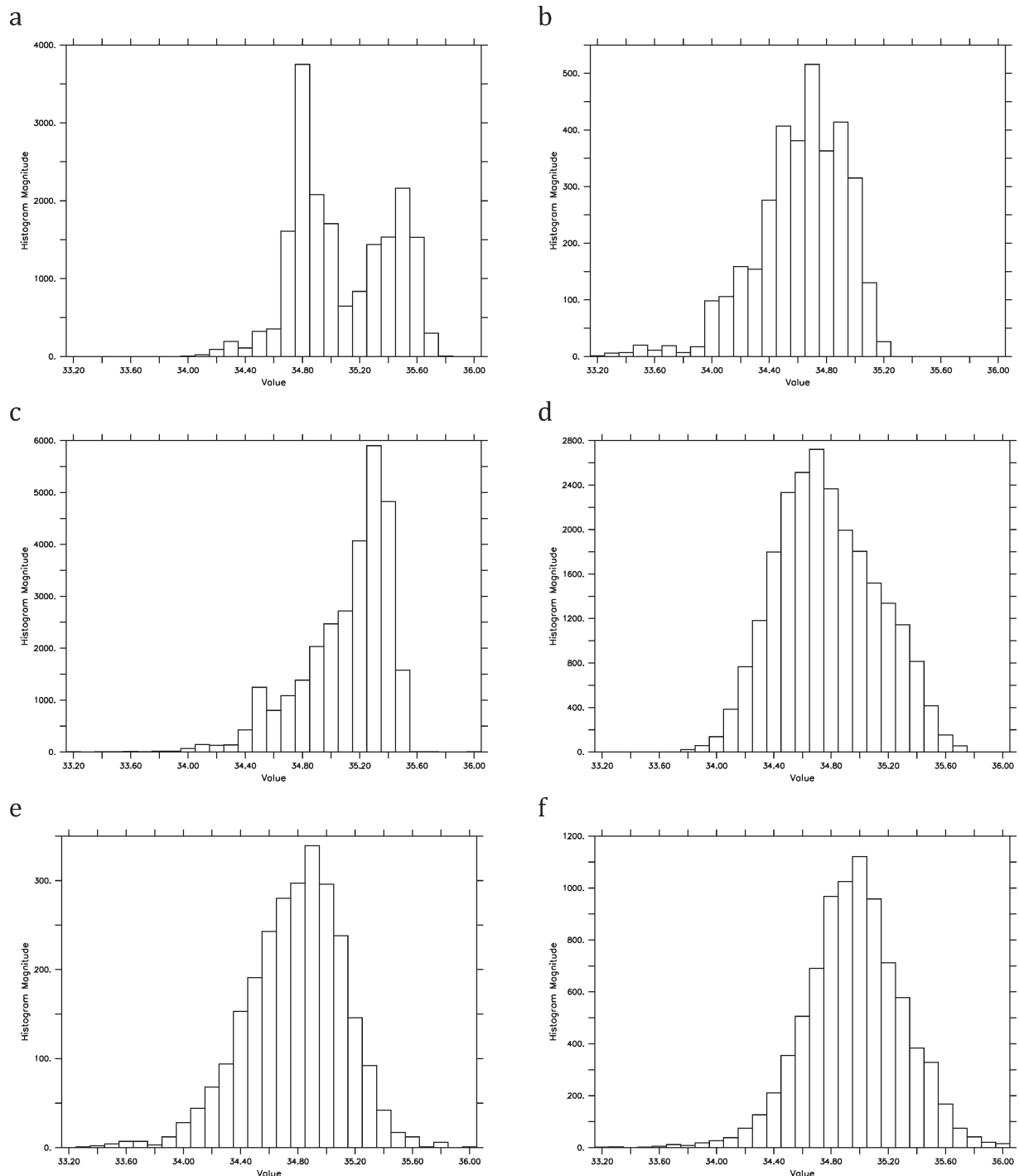
Figure 12. Frequency distribution of the amplitude of SSS (in psu) for (a) the 2010 TSG data, (b) the time series data at the Sabine Bank, (c) the drifter data, (d) the gridded product over the Coral Sea region, (e) the Aquarius, and (f) SMOS satellite missions. Statistics relative to these different figures are given in the Table 2.

features at the scale of mesoscale eddies (∼100 km) varies from about −1.1 to +0.6 psu in SSS (Table 1). These values are much larger than the amplitudes (∼0.2–0.3) typically found for the first harmonic of climatological estimates of SSS in the Coral Sea [i.e., *Boyer and Levitus*, 2002]. With a smaller amplitude as compared to the freshpool front in the eastern Pacific off the Panama coasts [*Alory et al.*, 2012], we also observed the seasonal displacement of a sharp salinity front that bounds warm and fresh

waters of the Western Pacific Warm Pool (WPWP). This frontal characteristic is quite similar to the salinity front at the eastern edge of the equatorial WPWP [*Picaut et al.*, 1996; *Maes et al.*, 2004]. However, an important distinction between these two signals is the predominance of seasonal variability in the Coral Sea, while the dominant variability along the equator is interannual in relation to ENSO [i.e., *Maes et al.*, 2010]. The questions to be addressed would be whether these migrations have an

Table 2. Statistics for the SSS Distributions in the Coral Sea as Shown in Figure 12[a]

|	Number of Data	Mean Value	Standard Deviation	Median Value	Skewness
TSG Data (2010)	18,682	35.08	0.11	34.97	+0.04
Drifters Data (2010)	29,087	35.10	0.09	35.20	−2.10
Sabine Bank (2000–2009)	3433	34.61	0.10	34.66	−0.90
Gridded Product (2000–2009)	23,520	34.77	0.12	34.74	+0.17
Aquarius[b] (8/2011–8/2012)	2624	34.77	0.11	34.81	−0.45
SMOS[b] (8/2011–8/2012)	8547	34.96	0.11	34.96	−0.18

[a]Values relative to salinity are given in psu.
[b]The domain for the satellite products is 18–13°S/155–165°E, where there are no lands.

influence on the onset of the Australian summer monsoon [*Kawamura et al.*, 2002] or on the propagation of large-scale disturbances like the MJO. It would be important to extend the study into the western part of the Coral Sea up to the Australian coast to the Great Barrier Reef, where the ecosystem is highly sensitive to climate change [*Wachenfeld et al.*, 2007].

[19] Several physical processes have been suggested that might generate the small-scale features in SST and SSS, including rainfall events, stirring by mesoscale eddies, and coupled air-sea responses to intraseasonal variability such as the MJO. At least, two other processes that could produce variations with similar amplitudes should also be included: changes in the vertical stratification within the top 10 m of the ocean and air-sea interactions at the diurnal period. *Henocq et al.* [2010] and *Reverdin et al.* [2012] have documented these variations in data collected in the Tropics. All these studies should be revisited and extended as more in situ data and more remotely sensed satellite data become available. The accuracy targeted by the SMOS and Aquarius satellite missions is 0.2 psu at the spatial scales between 50 and 150 km and time scales between weeks and months. In this context, small-scale features represent noise that needs to be understood to evaluate uncertainties in the satellite retrievals of SSS and to objectively map the satellite products.

[20] According to *Bingham et al.* [2002], the distribution of SSS in the Coral Sea is normally distributed, but it could result from the type of observations used to determine such distribution. To get a handle on some SSS features potentially due to differences in platforms and the timing and design of sampling rates, we considered different data sets. In addition to the TSG observations previously reported, it includes data from surface drifters released in the Coral Sea in 2010 [*Reverdin et al.*, 2012], from a gridded product for the 2000–2009 period described by *Delcroix et al.* [2011], and data from the SMOS and Aquarius satellite missions. Whenever it has been possible, the same period of time or the same regional domains have been considered. Depending on the source of the data, the distributions exhibit clearly distinct histogram characteristics (Figure 12 and relative statistics listed in Table 2). Several factors may be pointed out to explain such structural differences. The distribution resulting from the quasi-synoptic TSG data exhibits a bimodal structure that results
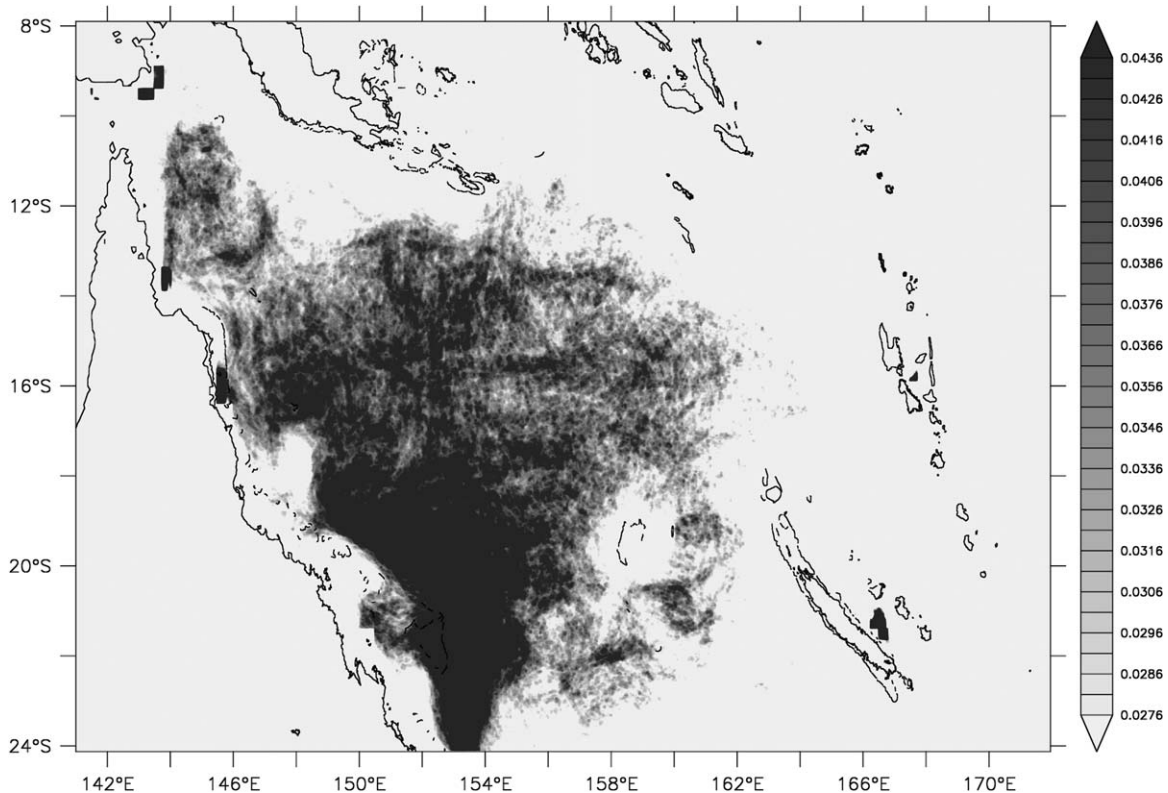
Figure 13. Annual mean of the FSLE field (in days^{-1}) for 2010 in the Coral Sea region.

from the sharp front separating the subtropical and equatorial waters of the Solomon Sea (Figure 1a). *Bingham et al.* [2002] discussed other examples of comparable non-Gaussian and bimodal distributions in the Gulf Stream. Even if the skewness value reported in Table 2 for the TSG data is small and positive (due to its bimodality), it is apparent that the distribution tails off toward the low values of SSS (Figure 12a). The distribution based on the surface drifters shows the greatest negative skewness, the second largest mean and the largest median. Both the shallow depth (∼1 m) and high frequency (every 30 min) of the drifter measurements may contribute to a better resolution of the diurnal cycle of the near-surface conditions, but the flow-following Lagrangian nature of the drifters is a factor as well. *Choukroun et al.* [2010] have shown that surface drifters are well suited to resolve the zonal mean circulation of the jets entering the Coral Sea, but they do not cross the frontal separation of water masses, as is the case for the ship-mounted TSG tracks. Because of its length and regular daily sampling, the distribution from the Sabine bank time series is probably the most stable, but it represents a single point. The most unusual distribution comes from the gridded product. There is an absence of low values, which have been probably smoothed out by the gridding procedure at monthly time periods. It also displays a large positive skewness (Table 2), which is not the result of a long tail. The reasons for this behavior are unclear, and could come from using a mixture of observations with different sampling biases or perhaps some of the observations are picking up the bimodal structure as do the TSG measurements. Finally, we note the satisfactory nature of both distributions of satellite data (Figures 12e and 12f), when they are compared to the Sabine bank distribution, both in terms of their mean, median, and negative skewness. Albeit there are some differences (lack of significant negative skewness as compared to drifters), this result suggests that remote satellite sensors may become very useful tools with which to investigate the full spatio-temporal variability of SSS, including in semienclosed regions like the Coral Sea.

[21] If describing the statistics of small-scales features is required for cross comparison of different data sets, understanding the physical mechanisms is also important. Daily maps of FSLE are useful for depicting short-lived processes and visualizing coherent structures, but if we average over long periods, we can also identify regions with different horizontal stirring activity [*Rossi et al.*, 2008]. As observed in many other regions, the stirring in the Coral Sea is not uniform and occurs at both small (∼10 km) and large (∼1000 km) scales. In the former case, the presence of coherent vortex structures mainly explains the filament-like structures observed in the FSLEs, while in the latter case, the dynamical features in the region may be related to regional circulation features in the stirring. If horizontal stirring intensity tends to increase with latitude at global scales [*Hernandez-Carrasco et al.*, 2012], we also observe a zonal dependency in the 2010 mean FSLE field between the eastern and western parts of the Coral Sea (Figure 13) within the 18°S and 12°S band of latitude. Southward of that band, typical higher values larger than 0.06 day^{-1} occur in the region close to the coast that is associated with the origins of the East Australian Current, values that are consistent with the case study of the Tasman Sea as reported by

Waugh et al. [2006]. In the center of the Coral Sea, nearby 16°S, the maximum extension of the highest activity should be associated with the high eddy variability resulting from barotropic instability due to the lateral shear between the eastward-flowing Coral Sea Countercurrent and its neighboring westward-flowing North Caledonian and North Vanuatu jets [*Qiu et al.*, 2009; *Gasparin et al.*, 2011]. As the intensity of the shear between these different jets fluctuates with latitude and with the season it results in a tendency to blur the zonal organization of the stirring. Eastward of 162°E the absence of significant stirring indicates that coherent Lagrangian structures at mesoscales are less active in the mean. It is nonetheless impossible to infer the potential role of submesoscale frontal dynamics (horizontal scales less than 10 km) with the present data.

[22] Spatial small-scale features are also inherently linked to the high-frequency variability. We showed that intraseasonal SST and SSS variability at the Sabine bank is dominated by the two regimes of variability, a "low-frequency" regime in the 30–70 days period band, likely resulting from MJO forcing and a "high-frequency" regime in the 10–30 days period band that may result from various processes (oceanic and atmospheric). Not surprisingly, the intraseasonal activity exhibits a marked seasonal cycle. However, there is little coherence of the seasonal spectrum between SST and SSS fields (see Figure 11), which suggests some possible processes at work at the intraseasonal time scales in this particular region. For instance, MJO-associated winds may alter SST through evaporation (or forced oceanic advection), whereas MJO-associated precipitation may impact the SSS more directly. Since the MJO interacts with both the synoptic scale so-called "convectively coupled equatorial waves" and the mesoscale convective systems that are prominent seasonally in the region of the Sabine bank, a strong relationship (i.e., in phase) between intraseasonal SSS variability and MJO activity is expected at seasonal time scale (Figure 11). The MJO imprint on the low-level circulation in this region is more ubiquitous (mostly because it is close to the SPCZ region which is characterized by a low-level convergence leading to ascending motion) and may explain that there is no apparent relationship between MJO activity and SST intraseasonal variability at the Sabine bank at seasonal time scale. Further work is needed to better understand this variability and it represents the focus of our current efforts.

[23] This study of small-scale features in surface fields of the Coral Sea was intended mainly to complement the ongoing analysis of remote sensing measurements that require in situ observations for calibration. It is thus important to ensure the ongoing collection of these data. At the same time, these data are also useful for understanding the impact of current changes in the oceanic environment on ecosystems and species [*Benhamou et al.*, 2011] and for placing current conditions in the context of long-term variations of past climates [*Gorman et al.*, 2012].

References

Alory, G., C. Maes, T. Delcroix, N. Reul, and S. Illig (2012), Seasonal dynamics of sea surface salinity off Panama: The far Eastern Pacific Fresh Pool, *J. Geophys. Res.*, *117*, C04028, doi:10.1029/2011JC007802.

Barton, I. J. (2007), Comparison of in situ and satellite-derived sea surface temperatures in the Gulf of Carpentaria, *J. Atmos. Oceanic Technol.*, *24*, 1773–1784.

Benhamou, S., J. Sudre, J. Bourjea, S. Ciccione, A. De Santis, and P. Luschi (2011), The role of geomagnetic cues in Green Turtle Open Sea navigation, *PLoS ONE*, *6*, e26672.

Bingham, F. M., S. D. Howden, and C. J. Koblinsky (2002), Sea surface salinity measurements in the historical database, *J. Geophys. Res.*, *107*(C12), 8019, doi:10.1029/2000JC000767.

Boyer, T. P., and S. Levitus (2002), Harmonic analysis of climatological sea surface salinity, *J. Geophys. Res.*, *107*(C12), 8006, doi:10.1029/2001JC000829.

Chen, J., R. Zhang, H. Wang, Y. An, P. Peng, and W. Zhang (2012), Isolation of sea surface salinity maps on various timescales in the tropical Pacific Ocean, *J. Oceanogr.*, *68*, 687–701.

Choukroun, S., P. V. Ridd, R. Brinkman, and L. I. W. McKinna (2010), On the surface circulation in the western Coral Sea and residence times in the Great Barrier Reef, *J. Geophys. Res.*, *115*, C06013, doi:10.1029/2009JC005761.

Delcroix, T., M. J. McPhaden, A. Dessier, and Y. Gouriou (2005), Time and space scales for sea surface salinity in the tropical oceans, *Deep Sea Res., Part I*, *52*(5), 787–813, doi:10.1016/j.dsr.2004.11.012.

Delcroix, T., G. Alory, S. Cravatte, T. Correge, and M. McPhaden (2011), A gridded sea surface salinity data set for the tropical Pacific with sample applications (1950–2008), *Deep Sea Res., Part I*, *58*(1), 38–48, doi:10.1016/j.dsr.2010.11.002.

Dewitte B., S. Illig, L. Renault, K. Goubanova, K. Takahashi, D. Gushchina, K. Mosquera, and S. Purca (2011), Modes of covariability between sea surface temperature and wind stress intraseasonal anomalies along the coast of Peru from satellite observations (2000–2008), *J. Geophys. Res.*, *116*, C04028, doi:10.1029/2010JC006495.

Donguy, J.-R. (1994), Surface and subsurface salinity in the tropical Pacific Ocean relations with climate, *Prog. Oceanogr.*, *34*, 45–78.

Fisher, M., B. Dewitte, and L. Maîtrepierre (2004), A non-linear statistical downscaling model: ENSO impact on precipitation over New Caledonia, *Geophys. Res. Lett.*, *31*, L16204, doi:10.1029/2004GL020112.

Freeman, L. A., A. J. Miller, R. D. Norris, and J. E. Smith (2012), Classification of remote Pacific coral reefs by physical oceanographic environment, *J. Geophys. Res.*, *117*, C02007, doi:10.1029/2011JC007099.

Gasparin, F., A. Ganachaud, and C. Maes (2011), A western boundary current east of New Caledonia: Observed characteristics, *Deep Sea Res., Part I*, *58*, 956–969.

Gorman, M. K., T. M. Quinn, F. W. Taylor, J. W. Partin, G. Cabioch, J. A. Austin Jr., B. Pelletier, V. Ballu, C. Maes, and S. Saustrup (2012), A coral-based reconstruction of sea surface salinity at Sabine Bank, Vanuatu from 1842 to 2007 CE, *Paleoceanography*, *27*, PA3226, doi:10.1029/2012PA002302.

Hendon, H. (2005), *Air-sea interaction, in Intraseasonal Variability in the Atmosphere-Ocean Climate System*, edited by W. K. M. Lau and D. E. Waliser, chap. 7, pp. 223–246, Springer, Heidelberg.

Hénin, C., and J. Grelet (1996), A merchant ship thermosalinograph network in the Pacific Ocean, *Deep Sea Res., Part I*, *43*, 1833–1856.

Henocq, C., J. Boutin, G. Reverdin, F. Petitcolin, S. Arnault, and P. Lattes (2010), Vertical variability of near-surface salinity in the tropics: Consequences for L-band radiometer calibration and validation, *J. Atmos. Oceanic Technol.*, *27*, 192–209, doi:10.1175/2009JTECHO670.1.

Hernández-Carrasco, I., C. López, E. Hernández-García, and A. Turiel (2011), How reliable are finite-size Lyapunov exponents for the assessment of ocean dynamics?, *Ocean Modell.*, *36*(3–4), 208–218, doi:10.1016/j.ocemod.2010.12.006.

Hernández-Carrasco, I., C. López, E. Hernández-García, and A. Turiel (2012), Seasonal and regional characterization of horizontal stirring in

the global ocean, *J. Geophys. Res.*, *117*, C10007, doi:10.1029/2012JC008222.

Huffman, G. J., et al. (2007), The TRMM multisatellite precipitation analysis (TMPA): Quasiglobal, multiyear, combined-sensor precipitation estimates at fine scale, *J. Hydrometeorol.*, *8*, 38–55.

Ioualalen, M., Y. Wakata, Y. Kawahara, Y. Gouriou, and D. Varillon (2003), Variability of the sea surface salinity (SSS) in the Western Tropical Pacific: On the ability of an OGCM to simulate the SSS, and on the sampling of an Operating Merchant Ship SSS network, *J. Oceanogr.*, *59*, 105–111.

Kawamura, R., Y. Fukuta, H. Ueda, T. Matsuura, and S. Iizuka (2002), A mechanism of the onset of the Australian summer monsoon, *J. Geophys. Res.*, *107*(D14), 4204, doi:10.1029/2001JD001070.

Klemas, V. (2011), Remote sensing of sea surface salinity: An overview with case studies, *J. Coastal Res.*, *27*(5), 830–838.

Leuliette, E. W., and J. M. Wahr (1999), Coupled pattern analysis of sea surface temperature and TOPEX/Poseidon sea surface height, *J. Phys. Oceanogr.*, *29*, 599–611.

Lin, J. W.-B., J. D. Neelin, and N. Zeng (2000), Maintenance of tropical variability: Impact of evaporation-wind feedback and midlatitude storms, *J. Atmos. Sci.*, *57*, 2793–2823.

Madden, R., and P. Julian (1972), Description of global-scale circulation cells in the tropics with a 40–50 day period, *J. Atmos. Sci.*, *29*, 1109–1123.

Maes, C., J. Picaut, and S. Belamari (2002), Salinity barrier layer and onset of El Niño in a Pacific coupled model, *Geophys. Res. Lett.*, *29*(24), 2206, doi:10.1029/2002GL016029.

Maes, C., J. Picaut, Y. Kuroda, and K. Ando (2004), Characteristics of the convergence zone at the eastern edge of the Pacific warm pool, *Geophys. Res. Lett.*, *31*, L11304, doi:10.1029/2004GL019867.

Maes, C., J. Picaut, and S. Belamari (2005), Importance of salinity barrier layer for the buildup of El Niño, *J. Clim.*, *18*, 104–118, doi:10.1175/JCLI-3214.1.

Maes, C., J. Sudre, and V. Garçon (2010), Detection of the eastern edge of the equatorial Pacific warm pool using satellite-based ocean color observations, *SOLA*, *6*, 129–132, doi:10.2151/sola.2010-033.

Picaut, J., M. Ioualalen, C. Menkes, T. Delcroix, and M. J. McPhaden (1996), Mechanism of the zonal displacements of the Pacific warm pool: Implications for ENSO, *Science*, *274*, 1486–1489.

Pierce, D. W., P. J. Gleckler, T. P. Barnett, B. D. Santer, and P. J. Durack (2012), The fingerprint of human-induced changes in the ocean's salinity and temperature fields, *Geophys. Res. Lett.*, *39*, L21704, doi:10.1029/2012GL053389.

Qiu, B., S. Chen, and W. S. Kessler (2009), Source of the 70-day mesoscale eddy variability in the Coral Sea and the North Fiji Basin, *J. Phys. Oceanogr.*, *39*, 404–420.

Reul, N. (2012), SMOS Level 3 SSS Research Products, Product User Document, Internal IFREMER and CNES document, pp. 21.

Reul, N., et al. (2013), Sea surface salinity observations from space with SMOS satellite: A new tool to better monitor the marine branch of the water cycle, *Surv. Geophys.*, *1–42*, doi:10.1007/GEOP-D-13-00003. http://link.springer.com/article/10.1007/s10712-013-9244-0.

Reverdin, G., S. Morisset, J. Boutin, and N. Martin (2012), Rain-induced variability of near sea-surface T and S from drifter data, *J. Geophys. Res.*, *117*, C02032, doi:10.1029/2011JC007549.

Reynolds, R. W., T. M. Smith, C. Liu, D. B. Chelton, K. S. Casey, and M. G. Schlax (2007), Daily high-resolution blended analyses for sea surface temperature, *J. Clim.*, *20*, 5473–5496.

Ridgway, K. R., and J. R. Dunn (2003), Mesoscale structure of the mean East Australian Current System and relationship with topography, *Prog. Oceanogr.*, *56*, 189–222.

Roemmich, D., and the Argo Steering Team (2009), Argo: The challenge of continuing 10 years of progress, *Oceanography*, *22*, 46–55, doi:10.5670/oceanog.2009.65.

Roemmich, D., and P. Sutton (1998), The mean and variability of ocean circulation past northern New Zealand: Determining the representativeness of hydrographic climatologies, *J. Geophys. Res.*, *103*, 13,041–13,054.

Rossi, V., C. Lopez, J. Sudre, E. Hernandez-Garcıa, and V. Garçon (2008), Comparative study of mixing and biological activity of the Benguela and Canary upwelling systems, *Geophys. Res. Lett.*, *35*, L11602, doi:10.1029/2008GL033610.

Schmitt, R. W. (1995), The ocean component of the global water cycle, U.S. National Report to IUGG, 1991–1994, *Rev. Geophys.*, *33*, 1395–1409.

Sudre, J., C. Maes, and V. Garcon (2013), On the global estimates of geostrophic and Ekman surface currents, *LOFE*, *3*, 1–20, doi:10.1215/21573689-2071927.

Takahashi, K., A. Montecinos, K. Goubanova, and B. Dewitte (2011), ENSO regimes: Reinterpreting the canonical and Modoki El Niño, *Geophys. Res. Lett.*, *38*, L10704, doi:10.1029/2011GL047364,.

Toole, J. M., and T. J. McDougall (2001), Mixing and stirring in the ocean interior, in *Ocean Circulation and Climate, Int. Geophys. Ser.*, vol. *77*, edited by G. Siedler, J. Church, and J. Gould, chap. 5.2, pp. 337–355, Academic, San Diego, CA.

Torrence, C., and G. Compo (1998), A practical guide to wavelet analysis, *Bull. Am. Meteorol. Soc.*, *79*, 61–78.

Wachenfeld, D., J. Johnson, A. Skeat, R. Kenchington, P. Marshall, and J. Ines (2007), Introduction to the Great Barrier Reed and climate change, in *Climate Change and the Great Barrier Reef*, edited by J. E. Johnson and P. A. Marshall, chap. 1, Great Barrier Reef Mar. Park Auth. and Aust. Greenhouse Off., Australia.

Waugh, D. W., E. R. Abraham, and M. Bowen (2006), Spatial variations of stirring in the surface ocean: the case study of the Tasman Sea, *J. Phys. Oceanogr.*, *36*, 526–542.

Wheeler, M., and H. H. Hendon (2004), An all-season real-time multivariate MJO index: Development of an index for monitoring, *Mon. Weather Rev.*, *132*, 1917–1932.

Yueh, S., W. Tang, A. Fore, A. Freedman, G. Neumann, J. Chaubell, and A. Hayashi (2012), Simultaneous salinity and wind retrieval using the CAP algorithm for Aquarius, paper MO4.5 presented at IEEE International Geoscience and Remote Sensing Symposium, Germany, 22–27 Jul., sponsored by ESA.